Materials Advances

ROYAL SOCIETY OF CHEMISTRY

PAPER

View Article Online
View Journal | View Issue

Cite this: *Mater. Adv.*, 2023, 4, 1546

Near ultraviolet light excitable highly efficient blue-green multicolour warwickite phosphor, $ScCaO(BO_3):Ce^{3+}, Tb^{3+}$†

Masato Iwaki, *[a] Haruto Sato,[a] Mizuki Watanabe, *[a] Kazuyoshi Uematsu,[b] Mineo Sato[b] and Kenji Toda[a]

Received 1st December 2022,
Accepted 12th February 2023

DOI: 10.1039/d2ma01065h

rsc.li/materials-advances

Ce^{3+}, Tb^{3+} co-doped multicolour emission phosphors show highly efficient green emission by energy transfer from Ce^{3+} to Tb^{3+}. However, an emission peak of near ultraviolet (UV) LEDs, which is around 390 nm, does not match the absorption wavelengths in most Ce^{3+}, Tb^{3+} co-activated phosphors. This spectral mismatch causes low emission efficiencies in phosphor-converted white LEDs (pc - wLEDs). In this study, Ce^{3+}, Tb^{3+} co-activated $ScCaO(BO_3)$ (SCBO) multicolour phosphors with the orthorhombic warwickite structure were successfully obtained by the conventional solid-state reaction method for the first time. The phosphors exhibit bright blue or green emission under near UV excitation around 390 nm due to energy transfer from Ce^{3+} to Tb^{3+}. In SCBO, Ce^{3+} and Tb^{3+} ions were substituted on two respective order sites, CaO_6 and ScO_6, leading to high emission efficiency. The internal quantum efficiency of SCBO : $0.01Ce^{3+}$, $0.15Tb^{3+}$ was reported to be 62% under the near UV excitation at 390 nm. In order to verify the potential of optical devices, particularly backlighting LEDs, the Rietveld refinement, photoluminescence properties, and decay curve analysis using the Inokuti–Hirayama model are described in this study.

Introduction

Phosphor-converted white light-emitting diodes (pc - wLEDs) have been utilized extensively in lighting and vehicle LED headlights.[1–4] Particular attention has been given to the use of the pc - wLEDs as a backlight source for liquid crystal displays (LCDs) due to their lower energy consumption and higher brightness.[5–10] Wide colour gamut and high luminous efficiency in pc - wLEDs provide the development of LCDs with improved properties. The wide colour gamut is obtained from an appropriate emission peak position with low full-width half maximum (FWHM) values in blue, green, and red components.[11] Commercial backlights of pc - wLEDs were constructed with blue-LEDs, green β-SiAlON:Eu^{2+}, and red $K_2SiF_6:Mn^{4+}$.[12] The emission peak position and FWHM value of the SiAlON:Eu^{2+} phosphor are at 540 nm and 54 nm, respectively. The FWHM value is somewhat greater than the target value (50 nm) of the Department of Energy (DOE), although the emission peak position is adequate for the target value (540 nm) of the DOE.[13] Narrow-band green-emission phosphors such as $RbLi(Li_3SiO_4)_2:Eu^{2+}$, $BaLi_2Al_2Si_2N_6:Eu^{2+}$, $Ba_2LiSi_7AlN_{12}:Eu^{2+}$, and γ -AlON:$Eu^{2+}$, Mn^{2+} [14–17] have been developed to achieve the DOE's target value for green emission phosphors. However, since these phosphors have challenges for practical use, the development of novel narrow green phosphors for pc - LEDs for the next-generation backlight is required.

Tb^{3+} is a promising green emission ion due to the 4f–4f electron forbidden transition because Tb^{3+}-activated phosphors show narrow-band green emission with an FWHM value of about 15 nm.[18] However, most Tb^{3+}-activated phosphors have a weak absorption band in the range of near UV to blue light.[19,20] An energy transfer phenomenon is one of the solutions to overcome the weak absorption in the near UV light region of Tb^{3+}.[21–23] The energy transfer occurs from donor ions to acceptor ions. As a result, the emission of both acceptors and donors is observed under the excitation of donors. Among the multicolour phosphors, Ce^{3+} is commonly used as the donor ion because its excitation band is more widely covered by the UV-light region, compared with other rare earth ions with sharp excitation bands. Furthermore, the emission efficiency of Ce^{3+} ions is higher than that of other rare earth ions owing to the

[a] *Graduate School of Science and Technology, Niigata University, 8050 Ikarashi 2-nocho, Niigata 950-2181, Japan. E-mail: f20k003j@mail.cc.niigata-u.ac.jp, mwatanabe@eng.niigata-u.ac.jp*

[b] *Department of Chemistry and Chemical Engineering, Faculty of Engineering, Niigata University, 8050 Ikarashi 2-nocho, Niigata 950-2181, Japan*

† Electronic supplementary information (ESI) available: Rietveld refinement, results of the Rietveld refinement, emission peak deconvolution, lists of the peak deconvolution, optical energy diagram, quantum efficiencies, and energy transfer efficiency. See DOI: **https://doi.org/10.1039/d2ma01065h**

5d–4f electric allowed transition of Ce^{3+}. Some Ce^{3+}, Tb^{3+} co-doped multicolour emitting phosphors have been developed: $LaOBr_3$:Ce^{3+}, Tb^{3+}, $LaPO_4$:Ce^{3+}, Tb^{3+} and $Ca_2Al_3O_6F$:Ce^{3+}, Tb^{3+}.[24–26] These multicolour phosphors show higher emission efficiency compared with only Tb^{3+}-activated luminescent materials due to Tb^{3+} accepting energy from Ce^{3+}. Nevertheless, Ce^{3+}, Tb^{3+} co-activated phosphors with high emission efficiency under near UV light excitation around 390 nm have not been developed because their photoluminescent properties are strongly dependent on the donor ion. Because the optical properties of Ce^{3+} ions vary depending on the host material, it is critical that for Ce^{3+}, Tb^{3+} co-activated multicolor emission phosphors for pc - wLEDs appropriate host materials are chosen.

Borate has been widely used in the phosphor host due to its low synthesis temperature, physical and chemical stabilities.[27,28] In particular, borates containing alkali earth and rare earth elements such as $Ba_3Y_2(B_2O_5)_3$, $Sr_3Gd_2(BO_3)_4$, $NaBaY(BO_3)_2$, and $Sr_2LiScB_4O_{10}$ are adopted as Ce^{3+}, Tb^{3+} co-doped multicolour phosphor hosts because their crystal structures consist of some substitutional sites for Ce^{3+} and Tb^{3+}.[29–32]

We focused on $ScCaO(BO_3)$ (SCBO) crystal structure that was first reported by Ma *et al.* from the single crystal X-ray diffraction, which is in agreement with warwickite such as $MgScO(BO_3)$, $YCaO(BO_3)$, and $Mg_{0.76}Mn_{1.24}O(BO_3)$, respectively.[33–36] The warwickite structure is composed of two disordered octahedral sites containing divalent (M^{2+}) and trivalent (M^{3+}) metal ions. The SCBO crystal structure contains CaO_6 and ScO_6 octahedra that are present, whereas, the other warwickite structures contain two disordered octahedra, $(M^{3+}/M^{2+})O_6$. Although $YCaO(BO_3)$:Ce^{3+}, Tb^{3+} with warwickite crystal structure has also been reported by Yang *et al.*, its emission efficiency was low.[37] Ce^{3+} and Tb^{3+} ions should be occupied on the two disordered $(Y/Ca)O_6$ sites in $YCaO(BO_3)$. Such an inhomogeneous distribution of emission ions leads to closer distances between donors or acceptors. As a result, the emission efficiency is low due to the excitation energy migration between donors or acceptors. On the other hand, two such distinct order sites in SCBO are expected to prevent the excitation energy migration between donors or acceptors because donor and acceptor ions may be replaced at each individual site. The luminescence properties of phosphors with the SCBO structure, on the other hand, have recently been reported; Ding *et al.* have reported on the energy transfer phenomenon from Ce^{3+} to Mn^{2+} of Ce^{3+}-activated SCBO and Wang *et al.* have reported the luminescent properties and internal quantum efficiency of Ce^{3+}-activated SCBO.[38,39] Although the luminescence properties of the SCBO-related phosphor were actively reported, the energy transfer phenomenon of Ce^{3+}, Tb^{3+} co-activated SCBO is unclarified.

In this study, we synthesized Ce^{3+}, Tb^{3+} co-activated SCBO and investigated their luminescence properties. The Rietveld analysis, photoluminescence, quantum efficiencies, and emission decay curve measurements were systematically conducted. These experimental consequences indicate that Ce^{3+}, Tb^{3+} co-doped SCBO phosphors show highly efficient narrow-band green emission excited by 390 nm, which is nearly close to near UV LEDs.

Preparation of materials

Non-doped and Ce^{3+}, Tb^{3+} co-doped SCBO were synthesized by the conventional solid-state reaction. Raw materials, Sc_2O_3 (Iwatani Sangyo, Co., Ltd., 99.999%), $CaCO_3$ (Kanto Chemical, Co., Inc., 99.5%), H_3BO_3 (Kanto Chemical, Co., Inc., 99.5%), CeO_2 (Kanto Chemical, Co., Inc., 99.99%) and Tb_4O_7 (Kanto Chemical, Co., Inc., 99.95%) were weighed in a ratio of $Sc:Ca:B:Ce:Tb = 0.99 - y: 1:1.1:0.01: y$ (y = 0, 0.01, 0.05, 0.10, 0.15 and 0.20), respectively; excess H_3BO_3 by 10 mol% over the stoichiometric ratio was added to suppress volatilization of B leading to impurities. The sorted raw materials were mixed in an agate mortar using acetone. After that, the mixtures were pressed into 1 mm diameter disk pellets under a 20 MPa pressure. The pelletized samples were placed within a BN crucible and heated at 1200 °C for 4 h in an N_2 atmosphere of 0.9 MPa by means of a vacuum and press sintering furnace (VESTA, Shimadzu Mectem. Inc.).

Characterization

Powder X-ray Diffraction (XRD) data on the obtained SCBO were collected using an X-ray diffractometer (D2 PHASER, Bruker; Co., Ltd.) with a monochromatic CuKα radiation (λ = 1.54056 Å) at 10 mA and 30 kV. The Rietveld refinement for the samples was carried out using the RIETAN-FP program software.[40] Photoluminescence (PL) and photoluminescence excitation (PLE) spectra of the samples were measured using a spectrofluorometer (FP-6500/FP-6600; Jasco Corp.) with a 150 W Xenon lamp. Absolute quantum efficiency (QE) of the samples was measured in an integrating sphere (ISF-834; Jasco Corp.) using a photoluminescence spectrometer (FP-8500; Jasco Corp.), where a standard halogen lamp (ESC-842; Jasco Corp.) was used for the calibration of this measurement system. Decay curves of the Ce^{3+} ion in the SCBO:0.01Ce^{3+}, $y$$Tb^{3+}$ phosphors were monitored using a Quantaurus-Tau (Hamamatsu Photonics Inc.). Chromaticity coordinate data for phosphors were measured at room temperature using a CCD camera (Hamamatsu C7473-36 PMA-11).

Results and discussion

Phase determination and crystal structure

Fig. 1 shows the XRD patterns of SCBO with and without emission ions. The simulation pattern of SCBO was calculated from the previously reported crystal information data.[33] The SCBO samples were in good agreement with the simulation pattern without any distinct impurity phases.

All the samples were obtained in a single phase with the orthorhombic SCBO structure. The Rietveld refinement was conducted for all the samples. Fig. 2 shows the fitting patterns obtained from the Rietveld refinement for the SCBO host, where a black cross symbol represents the observed data, a red solid line represents a calculated pattern, a blue line represents the difference between observed and calculated data and a green vertical line represents the Bragg position. The crystal information data of $ScCaO(BO_3)$ with an orthorhombic

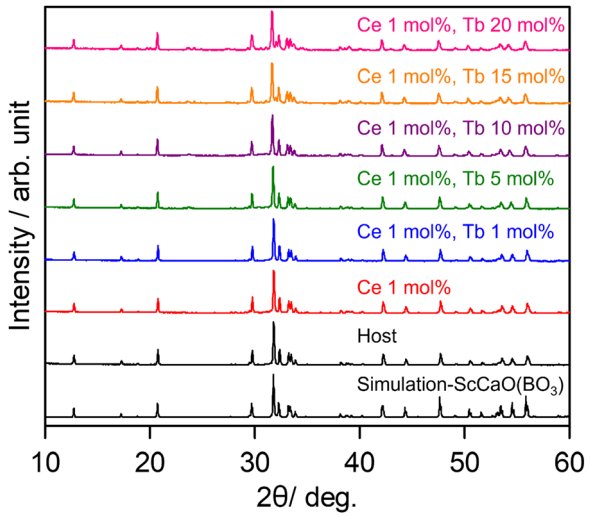

Fig. 1 XRD patterns of SCBO with and without emission ions.

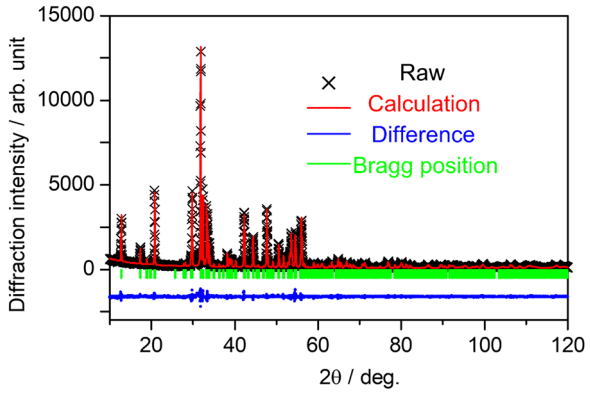

Fig. 2 Observed (black cross symbol), calculated (red) and difference (blue) obtained from Rietveld refinement on X-ray powder diffraction for SCBO.

structure in a space group of *Pnma* (No. 62), reported by Ma *et al.*,[33] was used as the model crystal structure. Table 1 demonstrates the crystallographic and *R*-values through the Rietveld refinement for SCBO. The *R*-values finally converged to R_{wp} = 9.418%, R_p = 6.803%, R_e = 5.717%, and S = 1.600, respectively, indicating that the high-purity SCBO was successfully obtained. R_{wp} values for all the samples were lower than 10% (See ESI,† Fig. S1 and Table S1). Table 2 shows the atomic coordination and isotropic atomic displacement of the SCBO host refined by the Rietveld analysis. The isotopic atomic displacement values, B_{eq} (Å^2), were estimated to be positive for all sites.

Fig. 3 shows the refined crystal structure of the SCBO along the *b* axis, as illustrated by the VESTA program.[41] As shown in Table 1, the lattice parameters are found to be a = 10.2544(4) Å, b = 3.3654(1) Å, c = 9.4159(3) Å and V = 324.94(2) Å^3. This crystal structure possesses one Sc site, one Ca site, one B site, and four O sites. Both Ca^{2+} and Sc^{3+} ions are coordinated by six O^{2-} ions and form independent octahedrons without disordering.

Table 1 Parameters refined through Rietveld analysis for SCBO host

Name	$ScCaO(BO_3)$
System	Orthorhombic
S. G.[a]	*Pnma* (#62)
a [Å]	10.2544(4)
b [Å]	3.3654(1)
c [Å]	9.4159(3)
V [Å^3]	324.94(2)
Z [−]	4
R_{wp} [%]	9.148
R_p [%]	6.803
R_e [%]	5.717
S [−]	1.600

[a] S. G. means space group.

Table 2 Atomic coordination and isotropic atomic displacement obtained through Rietveld refinement in SCBO host

Atom	Site	Occ.[a]	x	y	z	B_{eq} [Å^2]
Sc	4c	1	0.3905(1)	1.25	0.5728(1)	0.70(4)
Ca	4c	1	0.5890(1)	0.75	0.8401(1)	0.79(5)
B	4c	1	0.3086(9)	1.25	0.859(1)	1.4(2)
O1	4c	1	0.5005(4)	0.75	0.6121(5)	0.5(1)
O2	4c	1	0.2436(5)	1.25	0.7322(5)	1.4(1)
O3	4c	1	0.2652(4)	0.75	0.4920(5)	1.4(1)
O4	4c	1	0.4387(4)	0.25	0.8750(5)	1.8(1)

[a] Occ. is Occupancy.

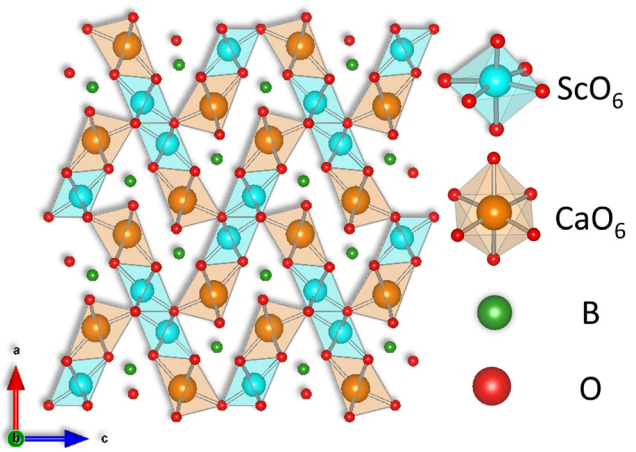

Fig. 3 Refined crystal structure of SCBO along *b* axis.

In addition, to understand the behavior of the substitution of Tb^{3+} for Sc^{3+}, the variations in the cell volume and lattice parameters are systematically summarized in Fig. 4(a)–(d). The lattice parameters of SCBO:0.01Ce^{3+}, $y$$Tb^{3+}$ (y = 0, 0.01, 0.05, 0.10, 0.15, and 0.20) are also listed in Table S1 (ESI†). According to Vegard's rule, the lattice volume of SCBO:0.01Ce^{3+}, $y$$Tb^{3+}$ expands linearly as the Tb^{3+} concentration increases. The *b* and *c* values, as well as the cell volume, are also elongated. The *a* value dramatically increased from 10.2601(3) Å to 10.2690(3) Å when SCBO:0.01Ce^{3+} incorporated 1 mol% of Tb^{3+}. As the Tb^{3+} concentration exceeds 1 mol%, the *a* value increased slightly

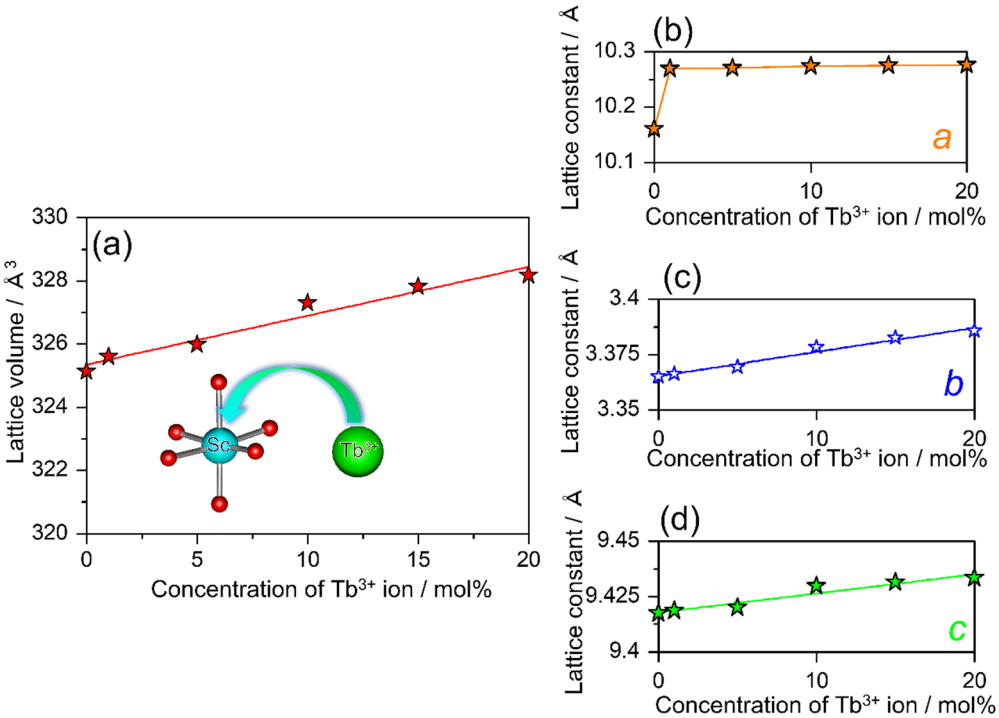

Fig. 4 Dependence of (a) the cell volume, lattice parameters, (b) *a*, (c) *b*, and (d) *c* on the concentration of Tb^{3+} ion in SCBO:0.01Ce^{3+}, *y*Tb^{3+} (*y* = 0, 0.01, 0.05, 0.10, 0.15, 0.20).

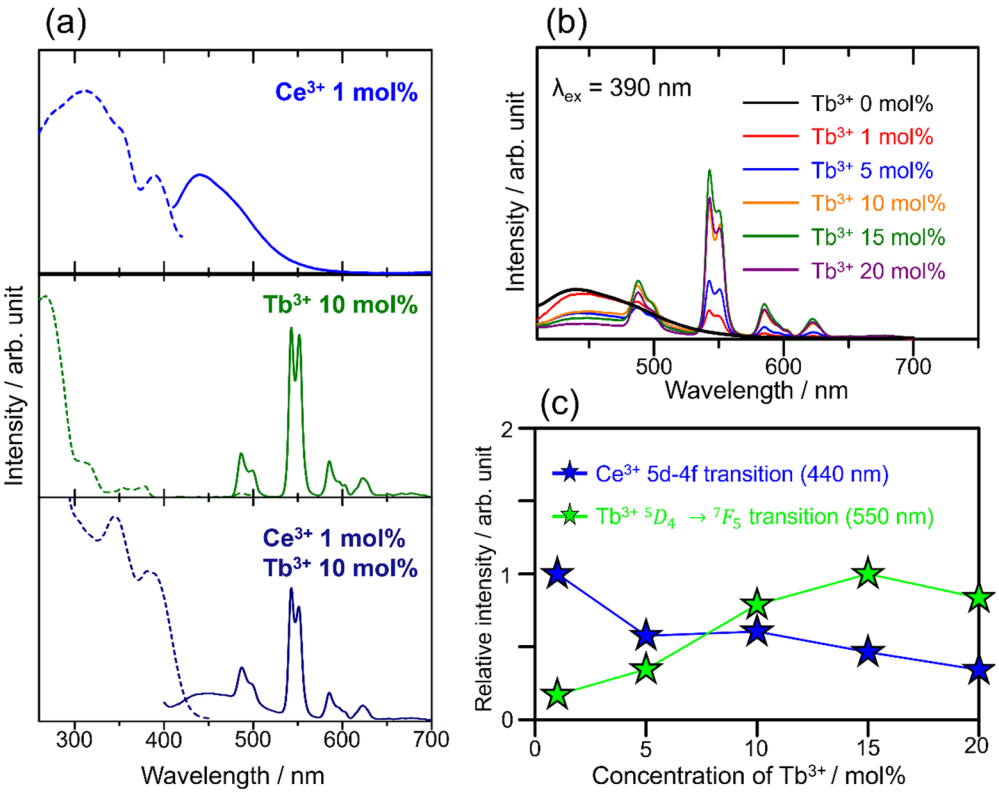

Fig. 5 (a) Photoluminescence excitation (dashed line) and emission (solid line) spectra of SCBO:0.01Ce^{3+} (above), SCBO:0.10Tb^{3+} (middle) and SCBO:0.01Ce^{3+}, 0.10Tb^{3+} (bottom). (b) Emission spectra of SCBO:0.01Ce^{3+}, *y*Tb^{3+} (*y* = 0, 0.01, 0.05, 0.10, 0.15, 0.20) under 390 nm excitation and (c) relative emission peak intensities in 5d-4f (Ce^{3+}; 440 nm) and $^5D_4$ → $^7F_5$ transitions (Tb^{3+}; 550 nm).

more than the b and c values. According to the relationship of the ionic radius, It is because the larger Tb^{3+} (0.923 Å; 6-fold coordination)[42] prefer to occupy smaller Sc^{3+} (0.745 Å; 6-fold coordination)[42] sites rather than the large Ca^{2+} (1.000 Å; 6-fold coordination).[42]

Photoluminescence properties of SCBO:Ce^{3+}, Tb^{3+}

The photoluminescence excitation (dashed line) and emission (solid) spectra of SCBO:0.01Ce^{3+} (above), SCBO:0.10Tb^{3+} (middle), and SCBO:0.01Ce^{3+}, 0.10Tb^{3+} (bottom) are shown in Fig. 5(a). Ce^{3+}-doped SCBO exhibits a broad blue emission with the peak top around 440 nm under near UV excitation at 390 nm, the emission spectrum was successfully deconvoluted into two components, as shown in Fig. S2 and Table S2 (ESI†). The energy difference between the peaks of the two deconvoluted spectra, corresponding to the electron transition from 5d to two ground states of the Ce^{3+} ion, $^2F_{5/2}$ and $^2F_{7/2}$,[43] was calculated to be 2169 cm^{-1}. This result indicates that the Ce^{3+} ion was replaced at one site in the SCBO structure. The excitation spectrum was also deconvoluted into three components with peaks around 300 nm, 350 nm, and 390 nm. The band with the peak around 300 nm was attributed to the host absorption because the band was observed in the absorption spectrum of the SCBO host; Ma *et al.* have reported that the band gap energy of the SCBO host was estimated to be 4.30 eV (= 288 nm).[34] The bands with peaks around 350 nm and 390 nm are attributed to the two excitation bands of the Ce^{3+} ion, the excitation bands are caused by the presence of the two ground states in the 4f–5d transition of the Ce^{3+} ion, as seen in other Ce^{3+}-doped phosphors such as YAG:Ce^{3+}.[44]

Site occupation of the Ce^{3+} ion in the SCBO structure was not revealed by the XRD analysis because the XRD patterns did not reflect the small amounts of Ce^{3+} added. To elucidate the emission mechanism of the Ce^{3+} ion in the SCBO structure, equations, suggested by Dorenbos, were adopted. Firstly, the centroid shift value ε_c was calculated using the following eqn (1);[45]

$$\varepsilon_c = 1.79 \times 10^{13} \sum_{i=1}^{N} \frac{\alpha_{sp}^{i}}{(R_i - 0.6\Delta R)^6} \quad (1)$$

where R_i means the bond distance [pm] between Ce^{3+} and O^{2-} atoms in a host lattice, ΔR represents the difference between ionic radii of Ce^{3+} and substitutional cations. N is the coordination number of Ce^{3+} with anions. α_{sp}^{i} shows the spectroscopic polarizability, estimated as the eqn (2);[46]

$$\alpha_{sp}^{i} = 0.33 + \frac{4.8}{\chi_{av}^2} \quad (2)$$

where χ_{av}^2 is the weighted average of electronegativity of cations in the crystal structure. χ_{av}^2 can be calculated from eqn (3);[47]

$$\chi_{av}^2 = \frac{1}{N_a} \sum_{i}^{N_c} \frac{z_i \chi_i}{\gamma} \quad (3)$$

N_a is the number of anions in the compound formula. N_c is the summation of cations in the crystal structure, $-\gamma$ and z_i are the charges of anion and cation i, respectively. χ_i is the electronegativity of the cation i, which is given by Allred.[48] From the eqn (2)–(3), χ_{av}^2, α_{sp}^{i} and ε_c are found to be 1.525, 2.394. Consequently, the centroid shift values of CaO_6 and ScO_6 sites were estimated to be 12 273 cm^{-1} and 36 034 cm^{-1}, respectively. Moreover, the crystal field splitting ε_{cfs} was estimated using the following eqn (4);[49]

$$\varepsilon_{cfs} = \beta_{poly}^{Q} R_{av}^{-2} \quad (4)$$

where β_{poly}^{Q} shows a constant depending on the shape and coordination number. In the case of SCBO, the octahedral $\beta_{octa} = 1.35 \times 10^{-9}$ pm^2 cm^{-1} was adopted.[50] R_{av} is the average bond length of the polyhedrons calculated by eqn (5);[51]

$$R_{av} = \frac{1}{N} \sum_{i=1}^{N} (R_i - 0.6\Delta R) \quad (5)$$

where R_i represents the bond distance between Ce^{3+} and O^{2-}, ΔR means the difference between ionic radii between the substitutional cation and Ce^{3+}. As a result, the crystal field splitting of Ce^{3+} in the CaO_6 site was found to be 24 350 cm^{-1}, while that in the ScO_6 site was 34 555 cm^{-1}. The Stokes shift value ΔS is simply explained using the following eqn (6);[52]

$$\Delta S = \lambda_{ex} - \lambda_{em} \quad (6)$$

where λ_{ex} and λ_{em} exhibit excitation and emission energies, respectively. ΔS value was found to be 2984 cm^{-1}. As a result, the ideal emission energy of Ce^{3+} in the CaO_6 and ScO_6 sites were found to be 24 342.9 cm^{-1} (411 nm) and −3500.0 cm^{-1} (−2857 nm), respectively, indicating that the observed emission band peaked around 440 nm of SCBO:0.01Ce^{3+} is close to the predicted emission energy in the CaO_6 site. Hence, Ce^{3+} is preferentially occupied on the CaO_6 site rather than the ScO_6 site; the optical energy diagram of Ce^{3+} in the CaO_6 polyhedron in the SCBO structure is shown in Fig. S3 (ESI†).

Fig. 5(a) middle shows the excitation and emission bands of 10 mol% Tb^{3+}-doped SCBO. The emission spectrum under excitation at 270 nm contains four notable emission peaks approximately at 488 nm ($^5D_4 \rightarrow {}^7F_6$), 550 nm ($^5D_4 \rightarrow {}^7F_5$), 585 nm ($^5D_4 \rightarrow {}^7F_4$), and 622 nm ($^5D_4 \rightarrow {}^7F_3$), corresponding to the 4f–4f electron-forbidden transition of Tb^{3+}. The excitation spectrum contains three components around 270 nm, 300 nm, and 320–370 nm. The highest energy band (270 nm) is owing to the charge transfer band between Tb^{3+} and O^{2-}. The second highest energy band (300 nm) belongs to the $4f^8 \rightarrow 4f^7 5d^1$ transition with the low spin state of Tb^{3+}.[53] The excitation band ranging from 320 nm to 370 nm shows the direct 4f–4f transition of Tb^{3+}. Tb^{3+}-doped SCBO shows strong luminescence under UV light excitation, but not under near UV light.

Ce^{3+}, Tb^{3+} co-doped SCBO exhibits a broad blue emission due to the 4f–5d transition of Ce^{3+} and narrow green emission due to the 4f–4f transition of Tb^{3+} under near UV light excitation. Fig. 5(b) shows the emission spectra of SCBO:0.01Ce^{3+}, $y$$Tb^{3+}$ (y = 0, 0.01, 0.10, 0.15, and 0.20) under near UV excitation at 390 nm. Fig. 5(c) also exhibits the relative peal emission intensities on the 5d–4f transition (440 nm) of Ce^{3+} and the

$^5D_4 \rightarrow {}^7F_5$ (550 nm) transition of Tb^{3+}. Until y = 0.15, the emission intensity of the $^5D_4 \rightarrow {}^7F_5$ (550 nm) transition of Tb^{3+} gradually increases, while that of the 5d–4f transition of Ce^{3+} remarkably decreases. This result suggests that the emission energy of Ce^{3+} as a donor ion transfers to Tb^{3+} as an acceptor ion, and that the energy transfer efficiency rises as Tb^{3+} concentration in SCBO increases. However, the emission intensity of SCBO:0.01Ce^{3+}, 0.20Tb^{3+} (y = 0.20) decreases compared to that in y = 0.15. This phenomenon implies that the energy migration among Tb^{3+} ions actively occurs.

The quantum efficiencies of SCBO:0.01Ce^{3+} and SCBO:0.01Ce^{3+}, 0.15Tb^{3+} are summarized in Table S3 (ESI†). Interestingly, the internal quantum efficiencies of SCBO:0.01Ce^{3+} and SCBO:0.01Ce^{3+}, 0.15Tb^{3+} were found to be 85% and 62%, respectively. Since Ce^{3+} and Tb^{3+} tend to be substituted on two different crystallographic sites, CaO_6 and ScO_6, respectively, the inhomogeneous distribution of Ce^{3+} and Tb^{3+} in the host lattice, leading to the excitation energy migration between Ce^{3+} and Tb^{3+}, would be suppressed. As a result, the emission efficiencies of SCBO:Ce^{3+}, Tb^{3+} became higher than those of $YCaO(BO_3)$:Ce^{3+}, Tb^{3+} with two disorder sites. Moreover, These values are higher than those of reported Ce^{3+}, Tb^{3+} co-doped multicolour emission phosphors such as $Sr_2LiScB_4O_{10}$:Ce^{3+}, Tb^{3+} (46%), $La_{0.59}Al_{2.03}B_4O_{10.54}$:$Ce^{3+}$, Tb^{3+} (41%), $Sr_5B_3O_9F$:Ce^{3+}, Tb^{3+}, Na^+ (57%) and $NaBaScSi_2O_7$:Ce^{3+}, Tb^{3+} (36%), indicating that SCBO:Ce^{3+}, Tb^{3+} has good potential for a near ultraviolet LED phosphor.[32,54–56]

Photoluminescence decay curve measurements and analysis

Fig. 6(a) shows the decay curves of SCBO:0.01Ce^{3+}, $y$$Tb^{3+}$ (y = 0, 0.01, 0.05, 0.10, 0.15, and 0.20) monitored at 443 nm under 405 nm excitation. The emission intensities of all samples decayed in a nanosecond (ns) order due to the 5d–4f electron-allowed transitions of Ce^{3+}. The enlarged view of the decay curves for the phosphors from 60 ns to 200 ns is also shown in Fig. 6(b). As the Tb^{3+} concentration increases, the emission attributed to the 4f–4f transition of Tb^{3+} decays rapidly because the probability of energy migration from Ce^{3+} to Tb^{3+} increases. Since it indicates that Ce^{3+} and Tb^{3+} are individually located on the CaO_6 site and ScO_6 site in SCBO, respectively, the lifetime τ was calculated using the eqn (7);[57–59]

$$I(t) = I_0 \exp\left(-\frac{t}{\tau}\right) \quad (7)$$

where $I(t)$ shows a photoluminescence emission intensity in a phosphor at the time t and I_0 means the initial emission intensity at t = 0. As a result, τ of SCBO:0.01Ce^{3+}, $y$$Tb^{3+}$ (y = 0, 0.01, 0.05, 0.10, 0.15, and 20) are found to be 36.2 ns, 34.7 ns, 33.7 ns, 30.1 ns, 29.7 ns, and 27.9 ns, respectively. The energy transfer efficiency η_T was calculated using the following eqn (8);[60–62]

$$\eta_T = 1 - \frac{\eta}{\eta_0} \quad (8)$$

where η_0 represents the emission efficiency of the donor ion without an acceptor ion, while η shows that with an acceptor ion. The concentration dependence of the energy transfer efficiency on Tb^{3+} in SCBO:0.01Ce^{3+}, $y$$Tb^{3+}$ is shown in Fig. S4 (ESI†), indicating that the η_T value steadily rises to around 49% in SCBO:0.01Ce^{3+}, 0.20Tb^{3+}. From these results, the energy transfer between Ce^{3+} and Tb^{3+} actively occurs upon increasing Tb^{3+} as an acceptor ion.

Energy transfer mechanisms are categorized into two theories: Dexter and Förster. Energy transfer in Dexter's theory is called the exchange interaction, while Förster's energy transfer phenomenon is electric multipole interaction. Identification of the energy transfer mechanism is to calculate the critical distance R_c between donor and acceptor ions, which is estimated by the eqn (9);[63,64]

$$R_c = 2\left[\frac{3V}{4\pi CN}\right]^{1/3} \quad (9)$$

where C is the total concentration of donor and acceptor ions. N means the number of substitutional cations for Ce^{3+} and Tb^{3+} ions in the SCBO structure. V is the cell volume. Consequently, the R_c values in SCBO:0.01Ce^{3+}, $y$$Tb^{3+}$ (y = 0.01, 0.05, 0.10, 0.15, and 0.20) are estimated to be 68.2 Å, 47.2 Å, 38.2 Å, 34.2 Å, and 31.2 Å, respectively. Exchange interaction dominantly occurs when the R_c values are below 5 Å, while electric multipole interaction predominately results beyond 5 Å. Because all the estimated critical

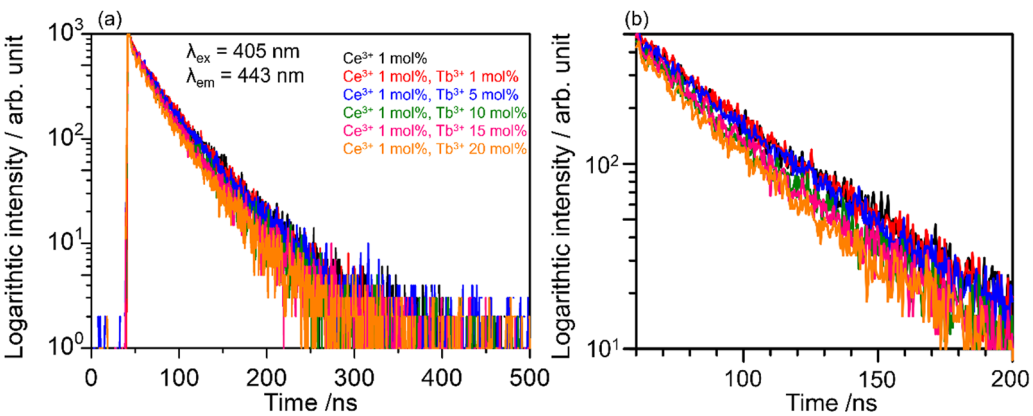

Fig. 6 (a) Photoluminescence decay curves of SCBO:0.01Ce^{3+}, $y$$Tb^{3+}$ (y = 0, 0.01, 0.05, 0.10, 0.15, 0.20) monitored 443 nm excited at 405 nm and (b) enlarged view of the decay curves between 60–200 ns.

distances in SCBO:0.01Ce^{3+}, yTb^{3+} are higher than 5 Å, Förster's energy transfer mechanism is dominated in SCBO:Ce^{3+}, Tb^{3+}.

In Förster's energy transfer mechanism, the electric multipole interaction is categorized into three types: dipole–dipole, dipole–quadrupole, and quadrupole–quadrupole interactions. To understand, in-depth, the multipole interaction in SCBO:Ce^{3+},Tb^{3+}, the Inokuti–Hirayama (I–H) model using the following eqn (10)[65] was adopted in this study.

$$I(t) = I_0 \exp\left[-\frac{\tau}{\tau_0} - \Gamma\left(1-\frac{3}{s}\right)C_0\left(\frac{\tau}{\tau_0}\right)^{\frac{3}{s}}\right] \qquad (10)$$

where $I(t)$ shows the emission intensity at a time t, I_0 means the initial intensity at $t = 0$, τ_0 is the lifetime of a donor ion without an acceptor ion, τ represents the donor lifetime including an acceptor ion, C_0 is the concentration ratio of an acceptor ion and critical transfer concentration ratio, s is the energy transfer type (s = 6; dipole–dipole, s = 8; dipole–quadrupole, s = 10; quadrupole–quadrupole), and $\Gamma\left(1-\frac{3}{s}\right)$ is the gamma function (s = 6; 1.77, s = 8; 1.43 and s = 10; 1.30), respectively. Based on this principle, we conducted the curve fitting for SCBO:0.01Ce^{3+}, 0.15Tb^{3+}, which are shown in Fig. 7. The indicator of the goodness-fit of decay curve fitting by means of the I–H model is determined by the figure of merit (FOM). Consequently, the FOM value is found to be the lowest value at 0.0898 in s = 8 (dipole–quadrupole). Many kinds of Ce^{3+}, Tb^{3+} co-doped phosphors exhibit the dipole–quadrupole interaction due to the energy transfer between Ce^{3+} with spin-allowed transition and Tb^{3+} with spin-forbidden transition.[66–70] Therefore, dipole–quadrupole interaction in SCBO:Ce^{3+}, Tb^{3+} is reasonable.

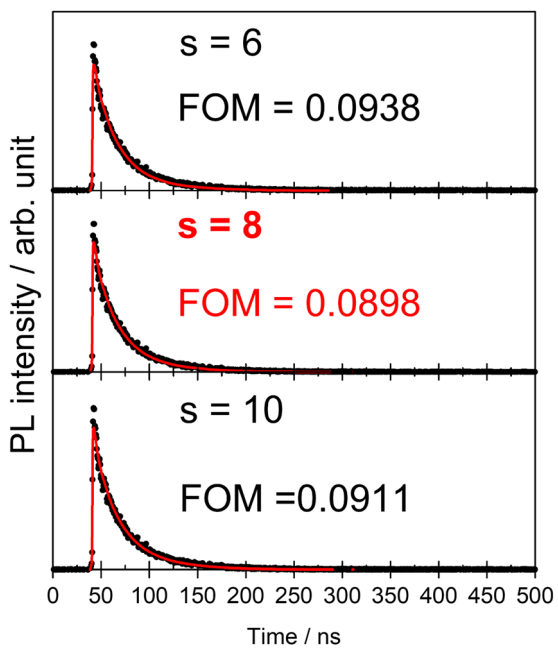

Fig. 7 Energy transfer analysis for SCBO:0.01Ce^{3+}, 0.15Tb^{3+} by Inokuti–Hirayama model in s = 6 (above), s = 8 (middle) and s = 10 (bottom).

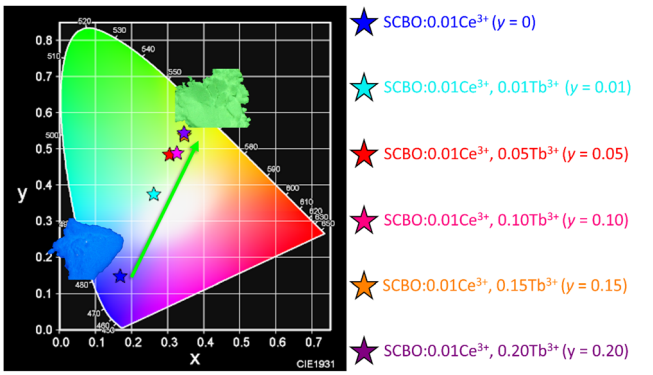

Fig. 8 Chromaticity diagram of SCBO:0.01Ce^{3+}, yTb^{3+} (y = 0, 0.01, 0.05, 0.10, 0.15, 0.20). Insert photographs show the blue-emitting SCBO:0.01Ce^{3+} and green-emitting SCBO:0.01Ce^{3+}, 0.15Tb^{3+}.

Table 3 Coordinate number (X, Y) of SCBO:0.01Ce^{3+}, yTb^{3+} (y = 0, 0.01, 0.05, 0.10, 0.15 and 0.20)

Sample	X	Y
y = 0	0.168	0.147
y = 0.01	0.261	0.374
y = 0.05	0.305	0.484
y = 0.10	0.325	0.488
y = 0.15	0.346	0.537
y = 0.30	0.345	0.544

Chromaticity diagram

Fig. 8 shows the chromaticity diagram of SCBO:0.01Ce^{3+}, yTb^{3+} (y = 0, 0.01, 0.05, 0.10, 0.15, and 0.20). The coordinate number (X, Y) of SCBO:0.01Ce^{3+}, yTb^{3+} are listed in Table 3. Ce^{3+}-doped SCBO exhibits a blue emission colour. On the other hand, as the Tb^{3+} concentration increases in SCBO:0.01Ce^{3+}, the location of (X, Y) coordination moves to the green region, indicating that the emission colour of SCBO:0.01Ce^{3+}, yTb^{3+} shifts dramatically from blue to green. This result indicates that the colour gamut of pc-LEDs can be tuned by adjusting the Tb^{3+} concentration in SCBO:Ce^{3+}.

Conclusion

Ce^{3+}, Tb^{3+} co-doped SCBO phosphors that are excited by near UV light were synthesized by the conventional solid-state reaction. Tb^{3+} preferentially occupies the ScO_6 sites because the Rietveld refinement for all samples revealed that the cell volumes and lattice constants, especially b and c, expanded with increasing Tb^{3+} concentration. Luminescence properties for the Ce^{3+}-doped SCBO phosphor revealed that Ce^{3+} ions are probably located on the CaO_6 octahedral. The blue-green multicolour emission band was observed in Ce^{3+}, Tb^{3+} co-doped SCBO under near UV excitation at 390 nm, indicating that energy transfer from Ce^{3+} to Tb^{3+} allows achieving phosphors that are excited by near UV light, while Tb^{3+}-doped SCBO did not show a strong green emission under near UV light. In particular, the internal quantum efficiencies of SCBO:0.01Ce^{3+}

(85%) and SCBO:0.01Ce^{3+}, 0.15Tb^{3+} (62%) were higher than those of reported Ce^{3+}, Tb^{3+} co-doped phosphors. Since Ce^{3+} and Tb^{3+} are replaced in each individual octahedral site without the disorder in the SCBO structure, leading to a homogeneous distribution of Ce^{3+} and Tb^{3+} in the SCBO lattice. The high quantum efficiencies of SCBO:Ce^{3+} and SCBO:Ce^{3+}, Tb^{3+} should be obtained due to the suppression of the excitation energy migration between the donors or the acceptors. Based on the results of the lifetime measurement and analysis, the probability of energy migration between Ce^{3+} and Tb^{3+} was enhanced with increasing Tb^{3+} concentration. Moreover, the lifetime analysis using the Inokuti–Hirayama model revealed that the dipole–quadrupole interaction dominantly occurs. Based on these measurements, Ce^{3+}, Tb^{3+}-doped SCBO has a good potential for near-ultraviolet LED phosphors. Moreover, the substitution of donors and acceptors for each individual site in the crystal structure is a useful design concept for highly efficient multicolour phosphors.

Conflicts of interest

There are no conflicts to declare.

Acknowledgements

Our research group thanks Prof. Dr Katsuyoshi Oh-ishi (Chuo University) for his assistance with the quantum yield measurements.

References

1 X.-J. Zhao, Y.-X. Cai, J. Wang, X.-H. Li and C. Zhang, *Appl. Therm. Eng.*, 2015, **75**, 248.
2 X. Long, J. He, J. He, J. Zhou, L. Fang, X. Zhou, F. Ren and T. Xu, *Renewable Sustainable Energy Rev.*, 2015, **41**, 29.
3 H. Lin, T. Hu, Y. Cheng, M. Chen and Y. Wang, *Laser Photonics Rev.*, 2018, **12**, 1700344.
4 Z. Xia and Q. Liu, *Prog. Mater. Sci.*, 2016, **84**, 59.
5 S. Li, R.-J. Xie, T. Takeda and N. Hirosaki, *ECS J. Solid State Sci. Technol.*, 2018, **1**, R3064.
6 R. Ma and P. Dai, *J. Lumin.*, 2022, **245**, 118772.
7 Y. Zhang, L. Luo, G. Chen, Y. Liu, R. Liu and X. Chen, *J. Rare Earths*, 2020, **38**, 1.
8 M. Zhao, Q. Zhang and Z. Xia, *Mater. Today*, 2020, **40**, 246.
9 L. Wang, X. Wang, T. Kohsei, K. Yoshimura, M. Izumi, N. Hirosaki and R.-J. Xie, *Opt. Express*, 2015, **23**, 28707.
10 L. Wang, R.-J. Xie, T. Suehiro, T. Takeda and N. Hirosaki, *Chem. Rev.*, 2018, **118**, 1951.
11 X. Zhang, H.-C. Wang, A.-C. Tang, S.-Y. Lin, H.-C. Tong, C.-Y. Chen, Y.-C. Lee, T.-L. Tsai and R.-S. Liu, *Chem. Mater.*, 2016, **28**, 8493.
12 M. Pattison, N. Bardsley, M. Hansen, L. Pattison, S. Schober, K. Stober, J. Tsao and M. Yamada, Solid-State Lighting 2017 suggested Research Topics Supplement: Technology and Context, DOE EERE, 2017.
13 S. Li, L. Wang, D. Tang, Y. Cho, X. Liu, X. Zhou, L. Lu, L. Zhang, T. Takeda, N. Hirosaki and R.-J. Xie, *Chem. Mater.*, 2018, **30**, 494.
14 M. Zhao, H. Liao, L. Ning, Q. Zhang, Q. Liu and Z. Xia, *Adv. Mater.*, 2018, **30**, 1802489.
15 Y. Wang, T. Seto, K. Ishigaki, Y. Uwatoko, G. Xiao, B. Zou, G. Li, Z. Tang, Z. Li and Y. Wang, *Adv. Funct. Mater.*, 2020, **30**, 2001384.
16 T. Takeda, N. Hirosaki, S. Funahashi and R.-J. Xie, *Chem. Mater.*, 2015, **27**, 5892.
17 L. Liu, L. Wang, C. Zhang, Y. Cho, B. Dierre, N. Hirosaki, T. Sekiguchi and R.-J. Xie, *Inorg. Chem.*, 2015, **54**, 5556.
18 Z. Hao, J. Zhang, X. Zhang, S. Lu and X. Wang, *J. Electrochem. Soc.*, 2009, **156**, H193.
19 R. Yantake, M. Kaiheriman, T. Yusufu and A. Sidike, *Sci. Rep.*, 2021, **11**, 5123.
20 G. A. Sotiriou, D. Franco, D. Poulikakos and A. Ferrari, *Nano Lett.*, 2012, **6**, 3888.
21 X. Zhang, L. Zhou, Q. Pang, J. Shi and M. Gong, *J. Phys. Chem. C*, 2014, **118**, 7591.
22 W. Lu, N. Guo, Y. Jia, Q. Zhao, W. Lv, M. Jiao, B. Shao and H. You, *Inorg. Chem.*, 2013, **52**, 3007.
23 K. Li, M. Shang, H. Lian and J. Lin, *J. Mater. Chem. C*, 2016, **4**, 5507.
24 X. Zhang, Y. Huang and M. Gong, *Chem. Eng. J.*, 2017, **307**, 291.
25 H. Meyssamy, K. Riwotzki, A. Kornowski, S. Naused and M. Haase, *Adv. Mater.*, 1999, **11**, 840.
26 Z. Xia and R.-S. Liu, *J. Phys. Chem. C*, 2012, **116**, 15604.
27 Y. Zhuo, S. Hariyani, J. Zhong and J. Brgoch, *Chem. Mater.*, 2021, **33**, 3304.
28 W. Xiao, X. Zhang, Z. Hao, G.-H. Pan, Y. Luo, L. Zhang and J. Zhang, *Inorg. Chem.*, 2015, **54**, 3189.
29 P. Wu, X. Tong, Y. Xu, J. Han, H. J. Seo and X. Zhang, *Opt. Mater.*, 2019, **91**, 246.
30 X. Fan, X. Sun, C. Liu, W. Tian, M. Li, Y. Luo and C. Wu, *J. Lumin.*, 2022, **242**, 118594.
31 W. Geng, X. Zhou, J. Ding and Y. Wang, *J. Am. Ceram. Soc.*, 2018, **101**, 4560.
32 H. Chen and Y. Wang, *Inorg. Chem.*, 2019, **58**, 7440.
33 R. Ma, D. Xu, Y. Yang, X. Su, B. Lei, Z. Yang and S. Pan, *Dalton Trans.*, 2017, **46**, 14839.
34 R. Norrestam, *Z. Kristallogr. - Cryst. Mater.*, 1989, **189**, 1.
35 Y. Zhang, X. L. Chen, J. K. Liang, T. Xu and Y. P. Xu, *J. Alloys Compd.*, 2001, **327**, 132.
36 N. V. Kazak, N. A. Belskaya, E. M. Moshkina, L. N. Bezmaternykh, A. D. Vasiliev, S. N. Sofronova, R. M. Eremina, E. V. Eremin, A. R. Muftakhutdinov, M. A. Cherosov and S. G. Ovchinnikonv, *J. Magn. Magn. Mater.*, 2020, **507**, 166820.
37 H. Yang, C. Li, Y. Tao, J. Xu, G. Zhang and Q. Su, *J. Lumin.*, 2007, **126**, 196.
38 J. Ding, M. Kuang, S. Liu, Z. Zhang, K. Huang, J. Huo, H. Ni, Q. Zhang and J. Li, *Dalton Trans.*, 2022, **51**, 9501.
39 W. Wang, T. Tan, S. Wang, S. Zhang, R. Pang, D. Li, L. Jiang, H. Li, C. Li and H. Zhang, *Mater. Today Chem.*, 2022, **26**, 101030.

40 F. Izumi, *The Rietveld Method*, ed. R. A. Young, *Oxford University Press*, Oxford, Ch. 13, 1993.
41 K. Monma and F. Izumi, *J. Appl. Crystallogr.*, 2011, **44**, 1272.
42 R. D. Shannon, *Acta Crystallogr., Sect. A: Cryst. Phys., Diffr., Theor. Gen. Crystallogr.*, 1976, **32**, 751.
43 Z. Xia and A. Meijerink, *Chem. Soc. Rev.*, 2017, **46**, 275.
44 G. Blasse and A. Bril, *J. Chem. Phys.*, 1967, **47**, 5139.
45 P. Dorenbos, *J. Lumin.*, 2003, **105**, 117.
46 P. Dorenbos, L. Pierron, L. Dinca, C. W. E. van Eijk, A. Kahn-Harari and B. Viana, *J. Phys.: Condens. Matter.*, 2003, **15**, 511.
47 P. Dorenbos, *Phys. Rev. B: Condens. Matter Mater. Phys.*, 2002, **65**, 235110.
48 A. L. Allred, *J. Inorg. Nucl. Chem.*, 1961, **17**, 215.
49 P. Dorenbos, *J. Phys.: Condens. Matter*, 2003, **15**, 4797.
50 P. Dorenbos, *Phys. Rev. B: Condens. Matter Mater. Phys.*, 2001, **64**, 125117.
51 P. Dorenbos, *ECS J. Solid State Sci. Technol.*, 2013, **2**, R301.
52 Y. Jia, A. Miglio, S. Ponce, X. Gonze and M. Mikami, *Phys. Rev. B*, 2016, **93**, 155111.
53 J. Ueda, S. Matsuishi, T. Tokunaga and S. Tanabe, *J. Mater. Chem. C*, 2018, **6**, 7541.
54 F. Junqin, J. Cao, Z. Li, Z. Li, J. Li, J. Lin, W. Li, Z. Mu and F. Wu, *Ceram. Int.*, 2019, **45**, 20316.
55 G. Li, Y. Wang, W. Zeng, W. Chen, S. Han, H. GuO and Y. Li, *J. Mater. Chem. C*, 2016, **4**, 3304.
56 S. Yang and S. Park, *J. Alloys Compd.*, 2020, **834**, 155094.
57 S. Liu, P. Sun, Y. Liu, T. Zhou, S. Li, R.-J. Xie, X. Xu, R. Dong, J. Jiang and H. Jiang, *ACS Appl. Mater. Interfaces*, 2019, **11**, 2130.
58 K. Li, M. Shang, D. Geng, H. Lian, Y. Zhang, J. Fan and J. Lin, *Inorg. Chem.*, 2014, **53**, 6743.
59 X. Zhang, L. Huang, F. Pan, M. Wu, J. Wang, Y. Chen and Q. Su, *ACS Appl. Mater. Interfaces*, 2014, **6**, 2709.
60 Z. Mazurak, M. Czaja, R. Lisiecki and J. Gabrys-Posarska, *Opt. Mater.*, 2011, **33**, 506.
61 X.-Y. Sun, S.-M. Huang, M. Gu, Q.-C. Gao, X.-S. Gong and Z.-P. Ye, *Phys. B*, 2010, **405**, 569.
62 X.-Y. Sun, M. Gu, S.-M. Huang, X.-L. Liu, B. Liu and C. Ni, *Phys. B*, 2009, **404**, 111.
63 G. Blasse, *Philips Res. Rep.*, 1969, **24**, 131.
64 R. Reisfeld, *Rare Earths*, *Springer*, *Berlin, Heidelberg*, 1991, p. 65.
65 M. Inokuti and F. Hirayama, *J. Chem. Phys.*, 1965, **43** 1978.
66 Z. Xia and W. Wu, *Dalton Trans.*, 2013, **42**, 12989.
67 X. Kang, S. Lu, H. Wang, D. Ling and W. Lu, *ACS Omega*, 2018, **3**, 16714.
68 H.-Y. Chung, C.-H. Lu and C.-H. Hsu, *J. Am. Ceram. Soc.*, 2010, **93**, 1838.
69 Q. Guo, L. Liao and Z. Zia, *J. Lumin.*, 2014, **145**, 65.
70 G. Li, S. Lan, L. Li, M. Li, W. Bao, H. Zou, X. Xu and S. Gan, *J. Alloys Compd.*, 2012, **513**, 145.